Dense Suspension Flow in a Penny-Shaped Crack, Part I : Theory

George R. Wyatt [a,*], Herbert E. Huppert [b]

[a] Emmanuel College, St. Andrew's Street, Cambridge, CB2 3AP, United Kingdom
[b] King's College, King's Parade, Cambridge, CB2 1ST, United Kingdom

A R T I C L E   I N F O

A B S T R A C T

We study the dynamics of proppants carried by fluid driven into an evolving penny-shaped fracture. During injection the slurry is modelled using a frictional rheology that takes into account the shear-induced migration and jamming of the proppants. Making pragmatic assumptions of negligible toughness and cross-fracture fluid slip, we find self-similar solutions supporting a range of proppant concentration profiles. In particular, we define an effective viscosity, which equates the fracture evolution of a slurry flow with a given proppant volume fraction, to a Newtonian flow with a particular viscosity. Using this framework, we are able to make predictions about the geometry of the growing fracture and the significance of tip screen-out. We are also able to model the closure of the fracture, after fluid pressure is released, and explore the effect of proppant concentration on the residual geometry of the fracture. The results have important applications to industrial fracking and geological dike formation by hot, intruding magma.

1. Introduction

Receiving a patent for his 'exploding torpedo' in 1865, US Civil War veteran Col. Edward Roberts established the practice of fracturing bedrock to stimulate oil wells (Wells, 2007). A technique, known as hydraulic fracturing, which uses pressurised fluid rather than explosives to develop fracture networks, only came into practice much later, in 1947 (Charlez, 1997), and is the topic of this paper. In particular, we will concentrate on the convective transport of proppants within an evolving cavity. These are small particles added to the fracturing fluid in order to prop open the developed fracture, which closes under far-field stress once the fluid pressure is released. Aside from its use in hydrocarbon recovery, hydraulic fracturing, or fracking, has uses including the measurement of in-situ stresses in rocks (National Earthquake Hazards Reduction Program (U.S.), Geological Survey (U.S.), 1983), generation of electricity in enhanced geothermal systems (Pierce, 2010) and improvement of injection rates in CO_2 sequestration (Miller, 2005). Hydraulic fracturing processes are also ubiquitous in geology: dikes and sills arise from cracks whose growth is driven by magma, with magmatic crystals taking the place of synthetic proppants. Phenomena such as crystallisation and gas exsolution in the cooling magma mean models of dike propagation vary widely, as is summarised in Rivalta et al. (2015). Notably, Petford and Koenders (1998) utilise granular flow theory to model the ascent of a granitic melt containing solids.

This paper combines two significant, but often disconnected, fields of fracking study, cavity flow and suspension flow:

- The study of (elastohydrodynamic) cavity flow focusses on the interplay between hydrodynamic properties of the fracturing fluid and material properties of the medium being fractured. In the zero-proppant case, the problem of a fluid-driven, penny-shaped crack requires the joint solution of a nonlinear Reynold's equation, which governs flow within the crack, and a singular

---

* Corresponding author.
  E-mail addresses: grw44@cam.ac.uk (G.R. Wyatt), heh1@cam.ac.uk (H.E. Huppert).

integral boundary condition, which takes into account the elastic properties of the surrounding medium. The general strategy used in this paper takes inspiration from the work of Spence and Sharp (1985), who, restricting to the two-dimensional case, were the first to solve these integro-differential equations. In particular, we will focus on cavities that keep the same shape in some evolving coordinate system, using series expansions to represent both the width and pressure profiles within the fracture. More recently, in 2002, Savitski and Detournay (2002) solved similar three-dimensional versions of these equations, allowing them to find fracture evolutions with simple time dependence in both the viscous and toughness dominated regimes. In the former, the principal energy dissipation is by viscous flow, and in the latter, energy dissipation is mostly by creating new fracture surfaces. Notably, the same paper (Savitski and Detournay, 2002) verifies that industrial fracking occurs in the viscous regime; this assumption makes the problem considered in this paper tractable to a semi-analytical approach.

- The mathematical study of suspension flow dates back to 1906, when Einstein used properties of suspensions to estimate the size of a water molecule (Einstein, 1906). In particular, he showed that very dilute particle-laden flows are Newtonian, with a viscosity which increases with the concentration of particles. However, during hydraulic fracturing it is necessary to model a full range of proppant volume fractions, which we denote by ϕ. It is typical to have both dilute flow near the crack walls, as well as plug flow at the centre of the cavity, where the slurry behaves as a porous granular medium. More recent experiments by Boyer et al. in 2011 (Boyer et al., 2011) investigate dense suspension rheology. They show that particles in suspension, subject to a constant normal particle pressure that is applied by a porous plate, expand when a shear is applied to the mixture. As a result, it is possible to write $\phi = \phi(I)$, where the dimensionless parameter, I, is the ratio between the *fluid* shear stress, which is proportional to the shear rate, and the particle normal stress. Likewise, fixing the solid volume fraction, they showed that the normal particle pressure is proportional to the applied shear stress. It is also shown that the constant of proportionality, μ, can be expressed as a monotonic function of ϕ. In the same paper (Boyer et al., 2011), forms of the rheological functions I and μ are suggested, showing good agreement with experimental data. Since then, several papers have suggested slightly different rheological models and are reviewed by Dontsov et al. in Dontsov et al. (2019a). These all feature a jamming limit, ϕ_m, which is the volume fraction at which the flowing slurry transitions into a granular solid. We will utilise the frictional rheology given by Garagash (2014), which is unique in allowing packings with $\phi > \phi_m$. These denser packings form due to 'in-cage' particle rearrangements caused by velocity and pressure fluctuations in the surrounding flow.

The current state of the art for modelling proppant flow in industrial hydraulic fractures utilises an advancement of the frictional rheology described in Boyer et al. (2011), due to Dontsov and Peirce (2014b), which includes gravitational settling, as well as proppant blocking in its description of the convective transport. This extended model is used by Dontsov et al. in Dontsov and Peirce (2014a) to explore the effect of proppant size during industrial fracturing and in Dontsov and Peirce (2015) to explore the effect of tip screen out. These papers use Khristianovich–Zheltov–Geertsma–De Klerk (KGD) and pseudo-3D (P3D) fracture geometries, about which more details can be found in Belyadi et al. (2019) and Zhang et al. (2017). In 2016, Shiozawa and McClure were able to apply similar techniques to the problem of a fully three-dimensional fracture (Shiozawa and Mcclure, 2016). We aim to extend findings from these papers to penny-shaped fracture geometries, which are less well studied, but physically relevant in shallow formations where overburden stress in the surrounding formation can become equal to the minimum horizontal stress (Belyadi et al., 2019).

The endeavours of this paper may be condensed into three main objectives. The first is to establish a mathematical framework that captures the behaviour of the proppant suspension as it interacts with the growing cavity. Here we will utilise a lubrication model, along with the assumption that the proppant flow is fully developed; equivalently, that the transverse fluid slip is negligible. Crucially, we will justify these assumptions using typical parameters from industrial fracking. We will also make a zero-toughness assumption, which is validated in Savitski and Detournay (2002). Once we have developed this framework, an important step will be to compare its features to those derived in the zero-proppant, viscosity dominated case by Savitski and Detournay (2002), particularly because we utilise a frictional rheology fitted to the dense regime (Boyer et al., 2011). Upon scaling, the equations we develop will be time independent, which means we can explore similarity solutions for the fracture shape and proppant distribution that have a power law time dependence.

The second objective is to find and examine accurate numerical solutions modelling the developing cavity, given a range of proppant concentrations. We will explore the empirical effects of changing proppant concentration on the geometry of the developing fracture, as well as the distribution of proppants. Using these semi-analytical solutions, we will be able to recover some of the main results of recent literature in hydraulic fracturing (Dontsov and Peirce, 2014a, 2015; Shiozawa and Mcclure, 2016), except in the context of a radial fracture. We will evaluate the consistency of our model in terms of potential shortfalls such as proppant screen-out near the crack tip and the breakdown of the continuum assumption. Since proppant screen-out relates directly to the growth and conductivity of the formulation, the diagnostics we develop for the severity of tip screen-out are significant in the context of industrial fracking.

The third, and final, objective is to leverage our results to make predictions about the geometry of the fracture after the fluid pressure is released. By assuming the remaining proppants are immobile and incompressible, we aim to establish simple formulae predicting the width and radius of the developed fracture. For the sake of brevity, this discussion will be left to Appendices D and E.

Aside from the availability of semi-analytical solutions, the problem of proppant flow in a penny-shaped crack is particularly appealing because of the potential of practical verification. Recent experiments by O'Keeffe et al. (2018) have explored fluid-driven, penny-shaped fractures in transparent, brittle hydrogels, making use of small particle concentrations to measure in-crack velocities. This paper is the first of two; the second of which will be a practical treatise on slurry driven-fractures in hydrogels, aiming to verify the predictions made here by repeating the experiments of O'Keeffe et al. (2018) including proppant concentrations.
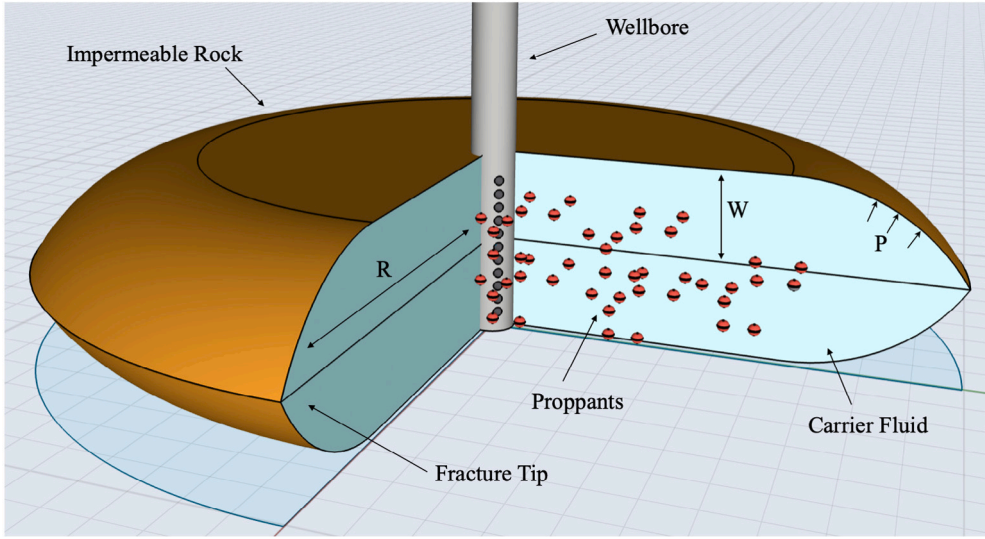
Fig. 1. Schematic of the penny-shaped crack.

2. Injection: Problem formulation

2.1. Fracture mechanics

We will use the framework of Savitski and Detournay (2002) to describe the interaction of the proppant-rich fluid and the surrounding elastic crack. We will make the following assumptions:

- The crack is axisymmetric and has reflectional symmetry in $z = 0$, with $w(r, t)$ defined as the half width and total radius $R(t)$, so $w(R, t) = 0$ (see Fig. 1).
- The fluid is injected from a line source, with the wellbore radius negligible compared to the fracture radius.
- The lag between the fracture tip and the fluid front is negligible compared to the fracture radius.
- The fracture propagates in continuous mobile equilibrium.
- The normal stress on the fracture walls due to proppants is negligible compared to the fluid pressure.

The third assumption is validated in the industrial context by Garagash and Detournay (2000) and Detournay and Garagash (2003), who show that, in this case, the length scale of the lag-region is considerably smaller than R and the solutions found for the development of the penny shaped fracture are similar. This assumption introduces a negative pressure singularity at the tip of the crack ($r = R$), taking the place of the region of vaporised fracturing fluid, or pore fluid, seen if a fluid lag is included in the model (Rubin, 1993; Detournay and Garagash, 2003); these details are discussed more in Appendix D. The fourth and fifth assumptions lead to the following integral equations from linear elastic fracture mechanics. These relate the net fluid pressure, $p(r, t)$, to the opening of the fracture and the toughness of the surrounding rock.

$$w(r,t) = \frac{4R}{\pi E'} \int_{r/R}^{1} \frac{y}{\sqrt{y^2 - (r/R)^2}} \int_{0}^{1} \frac{x p(xyR, t)}{\sqrt{1 - x^2}} \, dx \, dy, \tag{1}$$

$$K_{Ic} = \frac{2}{\sqrt{\pi R}} \int_{0}^{R} \frac{p(r,t)r}{\sqrt{R^2 - r^2}} \, dr, \tag{2}$$

where E' is the plane strain modulus, given by the Young modulus, E, and the Poisson ratio, ν, as $E' = E/(1 - \nu^2)$. K_{Ic} is the material toughness. These equations can be attributed to Sneddon (1951) and Rice (1968) respectively. We note that p represents the fluid pressure minus the in-situ stress of the surrounding rock, which is assumed to be isotropic. We write p with radial spatial dependence only; this will be validated later, along with the fifth assumption, using a lubrication argument.

2.2. Frictional Rheology

We model the injected flow as a Newtonian fluid containing identical spherical particles. Recent approaches in modelling dense slurry flow are characterised by empirical relations originally proposed by Boyer et al. (2011), which describe the shear thinning behaviour of such a fluid in a shear cell. This consists of a fluid, containing proppants, subject to a shear stress which is applied by

a porous plate. The first of these equations relates the shear rate to the normal stress, required to confine the particles to a fixed volume fraction; the second gives the ratio of the applied shear stress, from the porous plate, to the particle confining stress,

$$I(\phi) = \eta_f \dot{\gamma}/\sigma_n^s, \qquad\qquad\qquad \mu(\phi) = \tau/\sigma_n^s. \qquad (3)$$

Here η_f is the carrying fluid's dynamic viscosity; ϕ is the volume fraction of the proppants; $\dot{\gamma}$ is the solid shear rate; σ_n^s is the normal particle stress, which we will sometimes refer to as the particle pressure; and τ is the mixture shear stress. The second ratio is given the symbol μ, not to be confused with dynamic viscosity, because it resembles a friction coefficient. These relations are given a clear experimental grounding in Boyer et al. (2011), which is discussed in the introduction. Various forms of the dimensionless functions $I(\phi)$ and $\mu(\phi)$ have been compared to experimental results in Dontsov et al. (2019a) using the equivalent formulation: $\tau = \eta_s(\phi)\eta_f\dot{\gamma}$ and $\sigma_n = \eta_n(\phi)\eta_f\dot{\gamma}$, where $\eta_s = \mu(\phi)/I(\phi)$ and $\eta_n = 1/I(\phi)$.

In our calculations we will utilise the frictional rheology provided by Garagash (2014), which is unique in allowing packings with volume concentrations greater than ϕ_m. Here $I(\phi) = 0$, meaning the proppants have zero shear rate and effectively resemble a permeable solid. Explicitly, we use the expressions

$$\mu = \mu_1 + \frac{\phi_m}{\delta}\left(1 - \frac{\phi}{\phi_m}\right) + \left(I(\phi) + \left[\frac{5}{2}\phi_m + 2\right]I(\phi)^{0.5}\right)\left(1 - \frac{\phi}{\phi_m}\right)^2, \qquad (4)$$

$$I(\phi) = \begin{cases} \left(\phi_m/\phi - 1\right)^2 & \text{if } \phi < \phi_m \\ 0 & \text{if } \phi \geq \phi_m, \end{cases} \qquad (5)$$

where $\phi_m = 0.585$, $\mu_1 = 0.3$ and $\delta = 0.158$; these are plotted in Fig. 2. We might have used a different rheology, but this model shows good agreement with the data of Boyer et al. (2011) and Dagois-Bohy et al. (2015) for $0.4 < \phi < \phi_m$. Furthermore, owing to its linear extension beyond ϕ_m, μ is a simple monotonic function, meaning we can invert it easily to find ϕ. In other models $\phi(\mu)$ is constant for $\mu < \mu(\phi_m)$; this means that ϕ_m is the maximum volume fraction, regardless of how small shear stresses in the jammed slurry become. An important observation is that $\mu = 0$ implies $\phi = \phi_m + \delta\mu_1 \approx 0.63 \approx \phi_{rcp}$. Here ϕ_{rcp} is the random close packing limit, the maximal observed volume fraction due to random packing. This reflects the fact that, for a given confining stress, as the shear stress tends to zero, the particles pack to this maximal density.

This rheology uses a continuum model that requires particles to be small compared to the size of the fracture. This is in order to well-define the proppant volume concentration, ϕ. In our model the relevant ratio is that of the particle diameter to the typical crack width, the smallest cavity length scale. In Garagash (2014), good results are obtained using the same rheological model, with this ratio taking values as large as $1/10$. However, as the ratio approaches unity we have to consider non-local effects, such as proppant bridging across the crack width. This is particularly important near the fracture tip, where w approaches zero. These effects will be discussed in greater detail in Section 7, once we have formed a model of the evolving fracture. We must also be cautious applying these rheological models to dilute flows, since they are fitted to experimental data from the dense regime, where $\phi > 0.4$. This difficulty is somewhat inevitable, since the determination of I and μ requires measurement of the particle normal stress, or particle pressure, which becomes very small in the dilute regime.

2.3. Fluid slip

We define **u** as the slurry velocity, **v** as the particle velocity and $\mathbf{q} = \mathbf{u} - \mathbf{v}$ as the slip velocity. We then employ the slip relation

$$\mathbf{q} = \frac{a^2\kappa(\phi)}{\eta_f}\nabla\cdot\sigma^f, \qquad (6)$$

$$\kappa(\phi) = \frac{2(1-\phi)^{5.1}}{9\phi}, \qquad (7)$$

where a is the particle radius and σ_f is the fluid stress tensor. Since fluid and particle shear rates are often similar, we ignore fluid shear stresses and take $\sigma^f = -pI$; this is typical in the analysis of porous media flow. This simplifies (6) to Darcy's law. However, the effect of fluid shear stress is taken into account in the frictional rheology, where it is included as part of the mixture shear stress, τ. κ is a normalised form of the permeability of the solid particles; we use the function suggested by Garside and Al-Dibouni (1977), which is based on the phenomenology first described by Richardson and Zaki (1954). This choice of permeability function shows excellent agreement with the experimental results of Bacri et al. (1986).
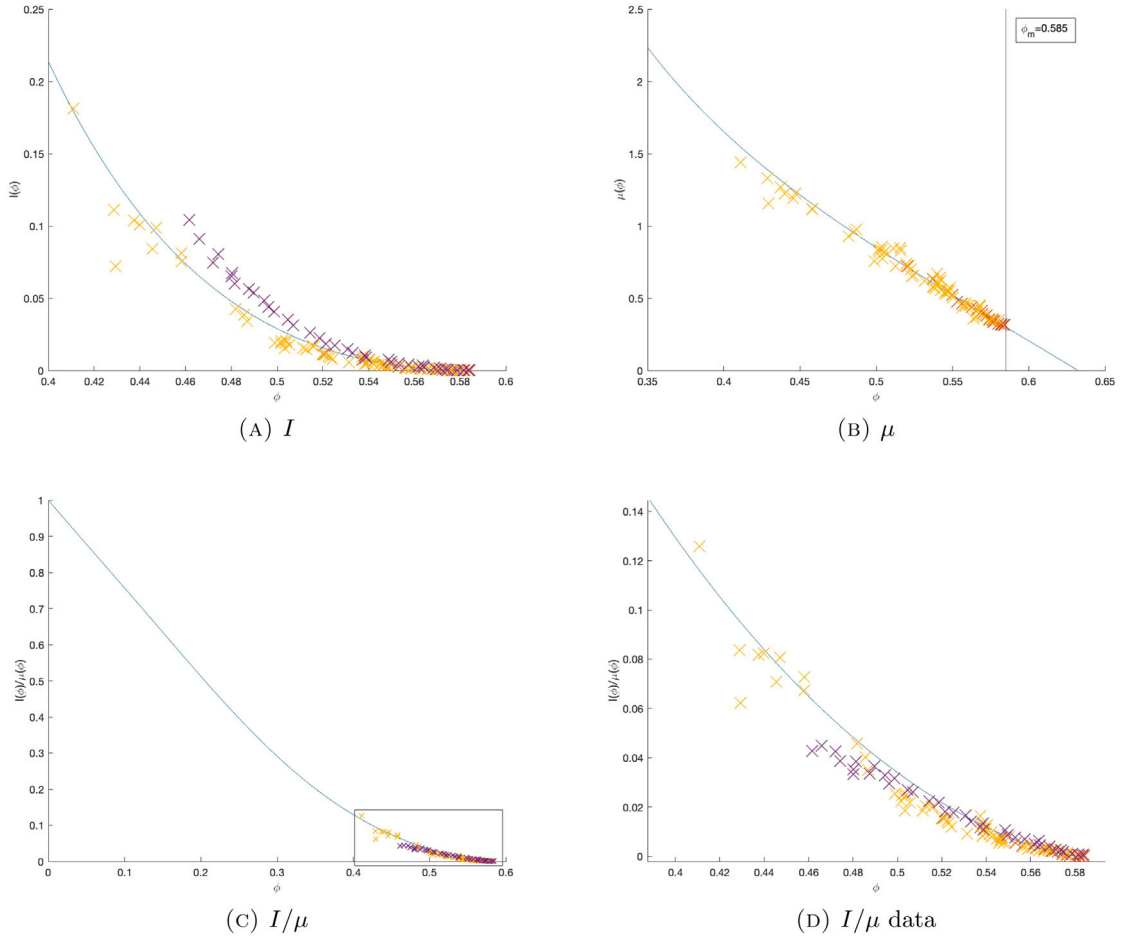
2.4. Conservation equations

We consider the effective Reynolds number,

$$\mathrm{Re}_{\mathrm{eff}} = \frac{\rho u_r w^2}{\eta_f R}, \qquad (8)$$

to be negligible. We also neglect the effect of gravity, since we are mainly concerned with small or neutrally buoyant proppants, which settle slowly. Hence, our momentum balance becomes

$$\nabla\cdot\sigma = 0. \qquad (9)$$

Fig. 2. Plots of the rheological functions I, μ and I/μ given by Garagash (2014). Also plotted is the experimental data of Boyer et al. (2011) using polystyrene spheres of diameter 580 μm in 2.15 Pa s fluid (red), as well as poly(methyl methacrylate) spheres of diameter 1100 μm suspended in 3.10 Pa s fluid (orange); and of Dagois-Bohy et al. (2015) using polystyrene spheres of diameter 580 μm suspended in 2.27 Pa s fluid (purple). All experiments are carried out with a fixed particle pressure, applied by a porous plate. (For interpretation of the references to colour in this figure legend, the reader is referred to the web version of this article.)

We also note that, subtracting the hydrostatic pressure term, we may write $\sigma = \tau - pI$. We then identify the components τ_{zz} and τ_{rz} with σ_n^s and τ respectively, from the equations in (3). For clarity we will write σ_{zz}^s instead of τ_{zz}, since this component is best though of as the normal particle containing stress. The assumption of axisymmetry then gives

$$\frac{1}{r}\frac{\partial(r\tau_{rr})}{\partial r} + \frac{\partial \tau_{rz}}{\partial z} - \frac{\partial p}{\partial r} = 0, \qquad\qquad \frac{1}{r}\frac{\partial(r\tau_{rz})}{\partial r} + \frac{\partial \sigma_{zz}^s}{\partial z} - \frac{\partial p}{\partial z} = 0. \qquad (10)$$

We also have the continuity equations

$$\nabla \cdot (\mathbf{v} + \mathbf{q}) = 0, \qquad\qquad \frac{\partial \phi}{\partial t} + \nabla \cdot (\phi \mathbf{v}) = 0. \qquad (11)$$

The first of these can be integrated over the fracture volume to give $Qt = 4\pi \int_0^R rw(r,t)dr$. Here, Q is the rate at which the slurry is pumped into the crack, which we will assume is constant. We will also assume that the proppants are injected at a constant rate, meaning the average concentration at the wellbore is constant.

3. Injection: Scalings

To help implement the assumptions of a lubrication model, where the crack width is far smaller than the crack radius, we introduce the scaled coordinates,

$$T = T(t), \qquad\qquad r = L(t)\Gamma(T)\xi, \qquad\qquad z = \epsilon(t)L(t)\eta.$$

Here $T(t)$ is the internal time scale, a monotonic function to be specified later; $L(t)$ gives the scaling in the radial direction; $\epsilon(t)$ is a small number, relating the width length scale to the radial length scale; and $\Gamma(T)$ is the crack radius, measured in the scaled coordinates, so $\xi = 1$ implies $r = R$. The use of an internal time scale, T, comes from the scaling choices made in Savitski and Detournay (2002), who derive governing equations for fracture development that involve two time dependent parameters. This means that, choosing T to equal one of these, one can address the two different modes of fracture propagation, where the energy dissipation is either toughness or viscosity dominated. We will take interest in the viscosity dominated regime, which is physically relevant to industrial fracturing, although we will work in generality until it is clear what our monotonic function should be. Analogously, we will choose ϵ and L later on to reflect the fact that we are modelling the viscosity dominated regime.

We scale the variables accordingly, using the frictional rheology, (3), and the slip equation, (6), to determine the scaling of q, τ and σ_s.

$$w(r,t) \to \epsilon L w(\xi, T), \qquad p(r,z,t) \to \epsilon E' p(\xi, \eta, T), \qquad R(t) \to L\Gamma(T),$$

$$v_z(r,z,t) \to -\dot{\epsilon} L v_z(\xi, \eta, T), \qquad\qquad v_r(r,z,t) \to \frac{-\dot{\epsilon} L}{\epsilon} v_r(\xi, \eta, T),$$

$$q_r(r,z,t) \to \frac{\epsilon}{L} \frac{a^2 E'}{\eta_f \Gamma} q_r(\xi, \eta, T), \qquad\qquad q_z(r,z,t) \to \frac{1}{L} \frac{a^2 E'}{\eta_f} q_z(\xi, \eta, T),$$

$$\tau(r,z,t) \to -\frac{\dot{\epsilon}}{\epsilon^2} \eta_f \tau(\xi, \eta, T), \qquad\qquad \sigma^s(r,z,t) \to -\frac{\dot{\epsilon}}{\epsilon^2} \eta_f \sigma^s(\xi, \eta, T).$$

The appearance of minus signs reflects the fact that ϵ, the ratio of the characteristic radius to the characteristic width of the fracture, is decreasing. We also assume the scaling is suitable so that all the scaled variables are $\mathcal{O}(1)$. Herein, we will use $\dot{()}$ for derivatives with respect to t and $(')$ for those with respect to T.

In the new, rescaled coordinates the equations describing the frictional rheology become $I(\phi) = \dot{\gamma}/\sigma_n^s$ and $\mu(\phi) = \tau/\sigma_n^s$. The slip equation becomes $\mathbf{q} = -\kappa(\phi)\nabla p$, where ∇ is now with respect to (ξ, η). The integral equations become

$$w(\xi, T) = \frac{4\Gamma}{\pi} \int_\xi^1 \frac{y}{\sqrt{y^2 - \xi^2}} \int_0^1 \frac{xp(xy,T)}{\sqrt{1-x^2}} dx dy, \qquad \aleph \equiv \frac{K_{Ic}}{\epsilon E' \sqrt{L}} = 2\sqrt{\frac{\Gamma}{\pi}} \int_0^1 \frac{p(\xi, T)\xi}{\sqrt{1-\xi^2}} d\xi. \qquad (12)$$

The momentum equations are

$$\frac{\epsilon}{\Gamma\xi} \frac{\partial(\xi\tau_{rr})}{\partial\xi} + \frac{\partial\tau_{rz}}{\partial\eta} + \frac{\epsilon^3 E' t}{\eta_f} \frac{\epsilon}{\dot{\epsilon} t\Gamma} \frac{\partial p}{\partial\xi} = 0, \qquad \frac{\epsilon^2}{\Gamma\xi} \frac{\partial(\xi\tau_{rz})}{\partial\xi} + \epsilon \frac{\partial\sigma_{zz}^s}{\partial\eta} + \frac{\epsilon}{\dot{\epsilon} t} \frac{\epsilon^3 E' t}{\eta_f} \frac{\partial p}{\partial\eta} = 0. \qquad (13)$$

Since we expect the radial pressure gradient to be comparable to the shear stress, τ_{rz}, we choose ϵ so that the dimensionless quantity $\epsilon^3 E't/\eta_f = 1$; this choice of scaling mirrors those used in Savitski and Detournay (2002) to model the regime where energy dissipation is mainly through viscosity. Finally, the global volume conservation equation then becomes $Qt/(\epsilon L^3) = 4\pi\Gamma^2 \int_0^1 \xi w(\xi, T)d\xi$, so in a similar manner we choose the dimensionless quantity $Qt/\epsilon L^3 = 1$. These choices mean

$$\epsilon(t) = (\eta_f/E')^{\frac{1}{3}} t^{-1/3}, \qquad L(t) = (E'Q^3/\eta_f)^{\frac{1}{9}} t^{4/9}. \qquad (14)$$

We will repeatedly use the relations $\dot{\epsilon}t/\epsilon = -1/3$ and $\dot{L}t/L = 4/9$. Using this choice of ϵ we note that, before scaling, $\sigma^s/p = \mathcal{O}(\epsilon)$; this validates the assumption that particle pressure is negligible compared to hydrostatic pressure at the crack walls. Also, by the scaled momentum equations,

$$\frac{\partial\tau_{rz}}{\partial\eta} = \frac{3}{\Gamma} \frac{\partial p}{\partial\xi} + \mathcal{O}(\epsilon), \qquad \frac{\partial p}{\partial\eta} = \frac{\epsilon}{3} \frac{\partial\sigma_{zz}^s}{\partial\eta} + \mathcal{O}(\epsilon^2), \qquad (15)$$

the second of which verifies the assumption that p has spatial dependence in the radial direction only. Because of the $\eta = 0$ reflectional symmetry, we note that $\tau_{rz}(\xi, 0) = 0$. So, ignoring $\mathcal{O}(\epsilon)$ terms and integrating ((15).1), we see that

$$\tau_{rz} = \frac{3\eta}{\Gamma} \frac{\partial p}{\partial\xi}, \qquad (16)$$

and, using the scaled equations from the frictional rheology,

$$\sigma_{zz}^s = \frac{3|\eta|}{\Gamma} \frac{1}{\mu(\phi)} \frac{\partial p}{\partial\xi}, \qquad \frac{\partial v_r}{\partial\eta} = \frac{3\eta}{\Gamma} \frac{I(\phi)}{\mu(\phi)} \frac{\partial p}{\partial\xi}. \qquad (17)$$

Then, using the condition $v_r(\xi, \pm w) = 0$, we deduce that

$$v_r(\xi, \eta) = -\frac{3}{\Gamma} \frac{\partial p}{\partial\xi} \int_\eta^w \frac{I(\phi)\eta}{\mu(\phi)} d\eta. \qquad (18)$$

4. Injection: Time regimes

In this choice of scaling, the slurry conservation equation becomes

$$\frac{1}{3\Gamma\xi} \frac{\partial(\xi v_r)}{\partial\xi} + \frac{1}{3} \frac{\partial v_z}{\partial\eta} + \left(\frac{a}{L\Gamma}\right)^2 \frac{1}{\epsilon^2\xi} \frac{\partial(\xi q_r)}{\partial\xi} + \left(\frac{a}{L}\right)^2 \frac{1}{\epsilon^4} \frac{\partial q_z}{\partial\eta} = 0. \qquad (19)$$

Table 1
Typical values of constants, given by Shiozawa and Mcclure (2016), Zhixi et al. (1997) and Liang et al. (2016).

Constant	Typical value
Q	$0.04 \ \mathrm{m^3 s^{-1}}$
E'	$40 \ \mathrm{GPa}$
η_f	$0.1 \ \mathrm{Pa \ s}$
ρ_f	$1000 \ \mathrm{kg \ m^{-3}}$
t	$10^3 \ \mathrm{s} - 10^6 \ \mathrm{s}$
K_{Ic}	$0.5 \ \mathrm{MPa \ m^{0.5}}$
a	$5 \times 10^{-5} \ \mathrm{m}$

Combining this with the scaled slip equation, noting (15), we obtain

$$\frac{1}{3\Gamma\xi}\frac{\partial(\xi v_r)}{\partial\xi} + \frac{1}{3}\frac{\partial v_z}{\partial\eta} - \frac{\epsilon\lambda}{\Gamma^2\xi}\frac{\partial}{\partial\xi}\left[\xi\kappa(\phi)\frac{\partial p}{\partial\xi}\right] - \frac{\lambda}{3}\frac{\partial}{\partial\eta}\left[\kappa(\phi)\frac{\partial\sigma_{zz}^s}{\partial\eta}\right] = 0. \tag{20}$$

Here $\lambda = a^2/(L^2\epsilon^3)$ is a constant; we will later identify it as the ratio of the fracture length scale to the development length scale, over which we expect proppant flow to stabilise.

We utilise the constants, relevant to hydraulic fracturing, given in Table 1. The values of Q, E', η_f, ρ_f and t are those used by Shiozawa & McClure in their recent simulation of a 3d hydraulic fracture (Shiozawa and Mcclure, 2016); the value of a represents a typical diameter for the finer proppants commonly used at the initiation of fracturing (Liang et al., 2016); the value of K_{IC} is the toughness of shale (Zhixi et al., 1997). This gives us the following estimates, where the value of $\mathrm{Re_{eff}}$ is calculated using formula (8), substituting each term with its typical scaling.

$$\epsilon \approx 1 \times 10^{-4} \cdot t^{-1/3}, \qquad\qquad L \approx 7 \times 10^0 \cdot t^{4/9},$$
$$\mathrm{Re_{eff}} \approx 3 \times 10^{-3} \cdot t^{-7/9}, \qquad\qquad \aleph \approx 4 \times 10^{-2} \cdot t^{1/9},$$
$$\lambda \approx 5 \times 10^1 \cdot t^{1/9}, \qquad\qquad a/(\epsilon L) \approx 6 \times 10^{-2} \cdot t^{-1/9}.$$

Considering the same problem in the zero-proppant case, Savitski and Detournay (2002) show that when $1.6\aleph < 1$, the fracture evolution is well approximated by taking the dimensionless toughness $\aleph = 0$; this inequality is certainly true for our estimate of $\aleph$, given the range of t we are interested in. Also, the choice $T = \aleph$ is taken, reflecting the dependence of the scaled solution on this monotonically increasing parameter; assuming $\aleph$ is negligible it is possible to neglect any T dependence. We will also use these assumptions, since toughness plays its greatest role in the process region, just beyond the crack tip (Detournay and Garagash, 2003), where proppants are likely to have little effect; moreover, the addition of proppants has an effect comparable to increasing viscosity, which would actually cause $\aleph$ to decrease. These choices mean that our model is relevant to the regime in which energy loss is dominated by viscous effects, rather than through the toughness of the surrounding medium; in Savitski and Detournay (2002) the transition between these modes is explored in detail and it is confirmed that industrial fracking occurs within the viscous regime.

Furthermore, for the time scales considered, ϵ and $\mathrm{Re_{eff}}$ terms are also very small, so can be ignored in keeping with our lubrication argument and the methods used in Savitski and Detournay (2002). Likewise $2a/(\epsilon L) < 1/10$, so the fracture is typically more than 10 particles wide. Garagash (2014), conclude that non-local phenomena such as proppant-bridging are not important in such cases; however we can still expect to see these effects near the narrow crack tip. The significance of this behaviour will be discussed in greater detail in Section 7.

We also note that λ is large; so in an effort to remove T dependence from our equations, justified at the end of this section, we shall neglect the first three terms in the continuity equation (20),

$$\frac{\partial}{\partial\eta}\left[\kappa(\phi)\frac{\partial\sigma_{zz}^s}{\partial\eta}\right] = 0. \tag{21}$$

This means we are effectively looking for solutions for the fracture shape, and proppant distribution, that grow with the scalings we have introduced, but are independent of the internal time scale, T. By the assumption of reflectional symmetry, the particle pressure gradient must vanish at $\eta = 0$. Because κ is generally non-zero, we deduce that the particle pressure is constant with η; and, by (17), so is $|\eta|/\mu(\phi)$. Hence,

$$\phi(\xi,\eta) = \mu^{-1}\left(\mu_w(\xi)\frac{|\eta|}{w(\xi)}\right), \tag{22}$$

where μ_w is an undetermined function of ξ, which we recognise as the value of μ at the crack wall. Noting that μ is a decreasing function, we see that μ_w also describes the rate at which the concentration drops from the centre to the wall of the cavity. We also notice that, in accordance to Dontsov et al. (2019b), we have plug flow in the centre of the channel, where concentrations are greater than ϕ_m. Because the slurry flows away from the wellbore, the distribution of proppants, which is described by μ_w, depends on the concentration of proppants in the injected mixture and how that changes with time. Hence, an important step in the determination of μ_w will be implementing the assumption that the average concentration at the wellbore is constant. This will be discussed in greater detail in Section 7.

It is interesting to note that (Garagash, 2014) experimentally verifies a length scale of $\epsilon^3 L^3/a^2$ for proppant flow in a channel, or pipe, to become fully established. This means the particle pressure gradient becomes negligible, and the cross fracture concentration profile becomes independent of the distance from the channel, or pipe, entrance. As a result, the constant $\lambda = a^2/(L^2\epsilon^3)$ can be interpreted as the ratio of the fracture length to the development length. Because this is large, an alternative route to (22) would have been to assume the transverse particle pressure is constant, as in Lecampion and Garagash's treatment of pipe and channel flow (Garagash, 2014), reflecting the full development of the flow. It is interesting to note that this assumption, and the assumption that λ is large, both lead to the same results, with the former arising from the consideration of proppant flow in non-radial geometries and the latter arising naturally from the scaling arguments we have implemented so far.

5. Injection: Governing equation for fracture width

In scaled coordinates, the governing equation for the conservation of proppant mass becomes

$$\frac{\xi \dot{L} t}{L}\frac{\partial \phi}{\partial \xi} + \left[\frac{\dot{\epsilon} t}{\epsilon} + \frac{\dot{L} t}{L}\right]\eta\frac{\partial \phi}{\partial \eta} = -\frac{\dot{\epsilon} t}{\epsilon \Gamma \xi}\frac{\partial(\xi \phi v_r)}{\partial \xi} - \frac{\dot{\epsilon} t}{\epsilon}\frac{\partial(\phi v_z)}{\partial \eta}. \tag{23}$$

Then, implementing our choices of ϵ and L, we obtain

$$\frac{4\xi}{3}\frac{\partial \phi}{\partial \xi} + \frac{\eta}{3}\frac{\partial \phi}{\partial \eta} = \frac{1}{\Gamma \xi}\frac{\partial(\xi \phi v_r)}{\partial \xi} + \frac{\partial(\phi v_z)}{\partial \eta}. \tag{24}$$

Integrating from $-w$ to w with respect to η, leaving details to Appendix A for brevity, we obtain

$$4\xi\frac{\partial}{\partial \xi}\left[w\Pi\circ\mu_w(\xi)\right] - w\Pi\circ\mu_w(\xi) = -\frac{9}{\Gamma^2\xi}\frac{\partial}{\partial \xi}\left[\frac{\xi w^3}{\mu_w(\xi)^2}\frac{\partial p}{\partial \xi}\Omega\circ\mu_w(\xi)\right]. \tag{25}$$

Here we have defined the rheological functions

$$\Pi(x) = \frac{1}{x}\int_0^x \mu^{-1}(u)du, \qquad\qquad \Omega(x) = \frac{1}{x}\int_0^x [\Pi(u)I\circ\mu^{-1}(u)u]du, \tag{26}$$

which we plot in Fig. 3.

Multiplying by ξ and integrating from ρ to 1, we obtain

$$\int_\rho^1 \xi w\Pi\circ\mu_w(\xi)d\xi + \frac{4}{9}\rho^2 w\Pi\circ\mu_w(\rho) = -\frac{\rho w^3}{\Gamma^2\mu_w^2}\frac{\partial p}{\partial \rho}\Omega\circ\mu_w(\rho), \tag{27}$$

which lends itself more easily to computation. Here we have taken $w^3\partial p/\partial\xi \to 0$ as $\xi \to 1$; this is physically motivated by the fact that this term is proportional to the radial flux, which vanishes at the crack tip. Moreover, Spence and Sharp (1985) show that, in the zero-proppant, zero-toughness regime, near the crack tip, $p \propto (1-\xi)^{-1/3}$ and $w \propto (1-\xi)^{2/3}$.

In order to compare this equation to the zero-proppant case, we assume μ_w is independent of ξ and take $\mu_w \to \infty$, to obtain

$$\int_\rho^1 \xi w(\xi)d\xi + \frac{4}{9}\rho^2 w = -\frac{\rho w^3}{\Gamma^2}\frac{\partial p}{\partial \rho}\lim_{\mu_w\to\infty}\left[\frac{\Omega(\mu_w)}{\mu_w^2\Pi(\mu_w)}\right]. \tag{28}$$

From Fig. 3c we deduce the right hand limit is approximately 2/5, which is confirmed exactly in Appendix B. Modelling the fluid as Newtonian, also leaving the details to Appendix B, we obtain the same equation, with a factor of 1/3 instead. We conclude that the equations governing Newtonian flow are not the same as those in the zero-proppant slurry flow limit. This is clearly a limitation of our approach, which arises from using a dense-fitted rheology in the dilute regime. However, the fact that the equations share a nearly identical form is promising, as we expect the qualitative behaviour of slurry flow to be similar to that of Newtonian flow.

6. Injection: Numerical solution

We implement the numerical method first used by Spence and Sharp (1985), with the adaptions of Savitski and Detournay (2002), to solve the equations we have derived so far. It will be useful to introduce $h(\xi) = w(\xi)/\Gamma$. The lubrication equation derived above, the elasticity equations and the global volume conservation equation become

$$\int_\rho^1 (\xi h\Pi\circ\mu_w)d\xi + \frac{4}{9}\rho^2 h\Pi\circ\mu_w = -\rho h^3\frac{\partial p}{\partial \rho}\frac{\Omega\circ\mu_w}{\mu_w^2}, \tag{29}$$

$$h(\xi) = \frac{4}{\pi}\int_\xi^1 \frac{y}{\sqrt{y^2-\xi^2}}\int_0^1 \frac{xp(xy)}{\sqrt{1-x^2}}dxdy, \tag{30}$$

$$0 = \int_0^1 \frac{p(\xi)\xi}{\sqrt{1-\xi^2}}d\xi, \tag{31}$$

$$1 = 4\pi\Gamma^3\int_0^1 (\xi h)d\xi. \tag{32}$$

(A) $\Pi(x)$ as a function of x

(B) $\Omega(x)$ as a function of x

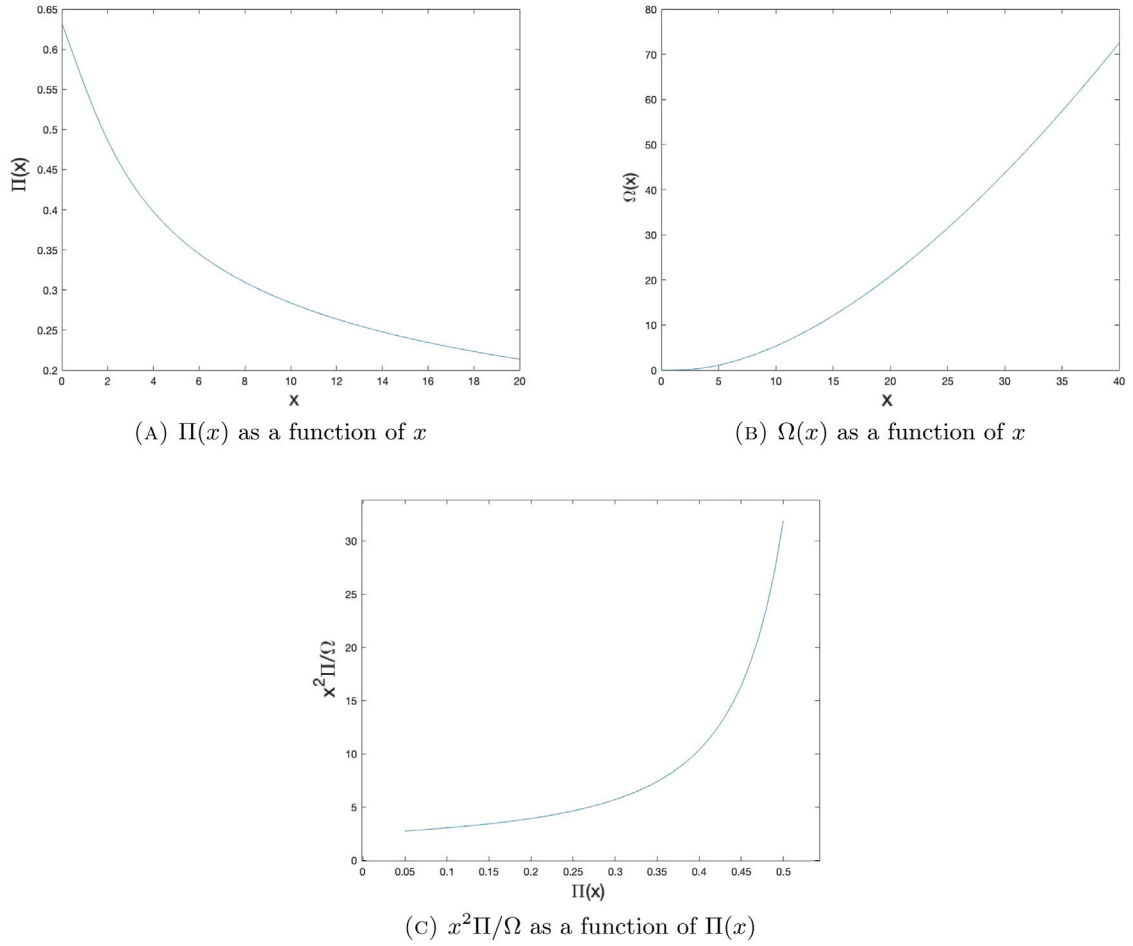(C) $x^2\Pi/\Omega$ as a function of $\Pi(x)$

Fig. 3. Plots of the rheological functions Π, Ω and $x^2\Pi/\Omega$.

These equations alone do not give unique solutions for $\{p, h, \mu_w\}$, so we will prescribe μ_w as part of the problem data. This allows us to uniquely determine a solution for $\{p, h\}$. We seek series approximations of the form

$$p(\xi) = \sum_{i=-1}^{N-1} A_i p_i(\xi), \qquad\qquad h(\xi) = \sum_{i=-1}^{N} B_i h_i(\xi), \qquad\qquad (33)$$

where we define

$$p_i(\xi) = \begin{cases} -\ln\xi + \ln 2 - 1 & (i = -1) \\ (1-\xi)^{-1/3} J_i(\frac{4}{3}, 2, \xi) + \omega_i & (i \geq 0) \end{cases}, \qquad h_i(\xi) = \begin{cases} \frac{4}{\pi}\left[(1-\xi^2)^{1/2} - \xi\cos^{-1}(\xi)\right] & (i = -1) \\ (1-\xi)^{2/3} J_i(\frac{10}{3}, 2, \xi) & (i \geq 0) \end{cases}.$$

Here the $i = -1$ terms are used to account for the logarithmic singularity in pressure at the inlet, expected as a result of the point source injection; the other terms allow for a general solution of (30). Importantly, we note that the p_i terms have a $(1-\xi)^{-1/3}$ singularity near the crack tip and the h_i terms are proportional to $(1-\xi)^{2/3}$ (for $i \geq 0$). This deliberately matches the asymptotic calculations from Spence and Sharp (1985), which arise from the assumptions of zero-lag and zero-toughness in an expanding hydraulic fracture. This allows the numerical method to converge accurately with few terms. The $J_i(p, q, \xi)$ are Jacobi Polynomials of order i defined on the interval $[0, 1]$, in the sense defined by Abramowitz and Stegun (1964), normalised to satisfy the orthonormality condition,

$$\int_0^1 (1-\xi)^{p-q}\xi^{q-1} J_i(p, q, \xi) J_j(p, q, \xi) d\xi = \delta_{ij}. \qquad\qquad (34)$$

This means that the h_i ($i \geq 0$) are orthonormal with respect to an inner product weighted by ξ. The ω_i are simply constants to ensure each of the p_i obey the zero-toughness equation; adding these constants means that the p_i lose their orthonormality properties, however this does not affect the solution finding process.

Because of its linearity, these series approximations reduce (30) to a linear equation,

$$B_i = \sum_{j=-1}^{N-1} P_{ij} A_j. \tag{35}$$

Here $(P)_{ij}$ is an $(N+2) \times (N+1)$ matrix whose entries we only have to calculate once by using the orthogonality relation given above, along with the fact that $\{p_{-1}, \theta_{-1}\}$ are a solution pair to (30). The entries of M, which can be found in Savitski and Detournay (2002), are listed in Appendix C for $N = 4$. The subtleties of calculating elements of P_{ij}, in the face of strong singular behaviour, are important and described in depth in Savitski and Detournay (2002). Finally, using the values of B_i given above, we assign a cost to each choice of A given by

$$\Delta(A) = \sum_{\xi \in \{0, 1/M, \ldots, 1\}} \left(\frac{\mathrm{RHS}(\xi; A)}{\mathrm{LHS}(\xi; A)} - 1 \right)^2. \tag{36}$$

This is calculated by considering the discrepancies between the left and right hand sides of (29), calculated at M + 1 equally spaced control points. We then minimise Δ with respect to A using the Nelder–Mead Simplex method (Lagarias et al., 1998).

7. Injection: Solutions for a constant μ_w μ_w

For monotonic choices of μ_w, the numerical method above shows good convergence. We see that the coefficients A_i and B_i drop off quickly with i, and the final value of Δ tends to zero rapidly as we increase N. If μ_w is a more complicated function, we may need to use a larger value of N, but good convergence is still possible. This is well illustrated by sinusoidal choices of μ_w, which require a value of N that grows linearly with the frequency of the function μ_w. This leads us to consider which choices of μ_w are most likely to appear in reality. We note that by (22),

$$\Pi \circ \mu_w(\xi) = \frac{1}{2w} \int_{-w}^{w} \phi(\xi, \eta) d\eta, \tag{37}$$

so we may view $\Pi \circ \mu_w(\xi)$ as the average proppant concentration at a given value of ξ. Since $\Pi \circ \mu_w$ is independent of time, we automatically satisfy the condition that the injection rates of the proppants and the fluid are constant. However this condition also means that the average concentration at the wellbore, $\Pi \circ \mu_w(0)$, must equal the average concentration taken by integrating over the entire crack volume. For a monotonic choice of μ_w this implies that μ_w must be independent of ξ. Herein we will make the assumption that μ_w is a constant and, as a result, so is $\Pi = \Pi(\mu_w)$. This is a natural assumption: at early times we do not expect significant concentration differences along the crack because radial length scales are small.

A great advantage of a constant Π is that we can define an 'effective viscosity', which we can absorb into our scaled variables the same way as we did with fluid viscosity. Under the assumption that μ_w is constant, (29) becomes

$$\int_{\rho}^{1} \xi h(\xi) d\xi + \frac{4}{9} \rho^2 h = -\frac{\rho h^3}{\eta_e} \frac{\partial p}{\partial \rho}, \tag{38}$$

where $\eta_e = \mu_w^2 \Pi / \Omega$ is what we call the effective viscosity. It is plotted in Fig. 3c, and is best thought of as a function of the average concentration, Π. Making the transformations

$$h = \eta_e^{1/3} \tilde{h}, \qquad\qquad p = \eta_e^{1/3} \tilde{p}, \qquad\qquad \Gamma = \eta_e^{-1/9} \tilde{\Gamma}, \tag{39}$$

our governing equations become

$$\int_{\rho}^{1} \xi \tilde{h} d\xi + \frac{4}{9} \rho^2 \tilde{h} = -\rho \tilde{h}^3 \frac{\partial p}{\partial \rho}, \quad \tilde{h}(\xi) = \frac{4}{\pi} \int_{\xi}^{1} \frac{y}{\sqrt{y^2 - \xi^2}} \int_{0}^{1} \frac{x \tilde{p}(xy)}{\sqrt{1 - x^2}} dx dy,$$
$$0 = \int_{0}^{1} \frac{\tilde{p}(\xi) \xi}{\sqrt{1 - \xi^2}} d\xi, \qquad 1 = 4\pi \tilde{\Gamma}^3 \int_{0}^{1} (\xi \tilde{h}) d\xi. \tag{40}$$

We will solve them using the numerical method described before, except with (40) in the place of (29)–(32).

Fig. 4 plots $\tilde{h}$ and $\tilde{p}$, calculated using $N = 4$ and $M + 1 = 501$ control points. Promisingly, we note that $\tilde{h} > 0$ and p shows the expected asymptotic behaviour. The value $\tilde{h}(0) = 1.36$ will be important in later discussion. The first column of Table 3 shows the coefficients A_i and B_i, as well as the calculated value of $\tilde{\Gamma} = 0.598$. Significantly, we see that A_i and B_i decrease rapidly with i, suggesting that a solution with higher order terms is unnecessary. This is supported by the small value of $\Delta \approx 5 \times 10^{-5}$, with evenly spread contributions from control points along the radius of the crack. This suggests that we have found a genuine solution, and that the tip asymptotics are indeed suitable.

We now focus on finding numerical solutions for different concentrations in order to consider features such as the velocity profile and proppant distribution within the cavity. We consider the case of four different values of the average concentration, Π. These are given in Table 2, along with the corresponding values of μ_w and η_e.
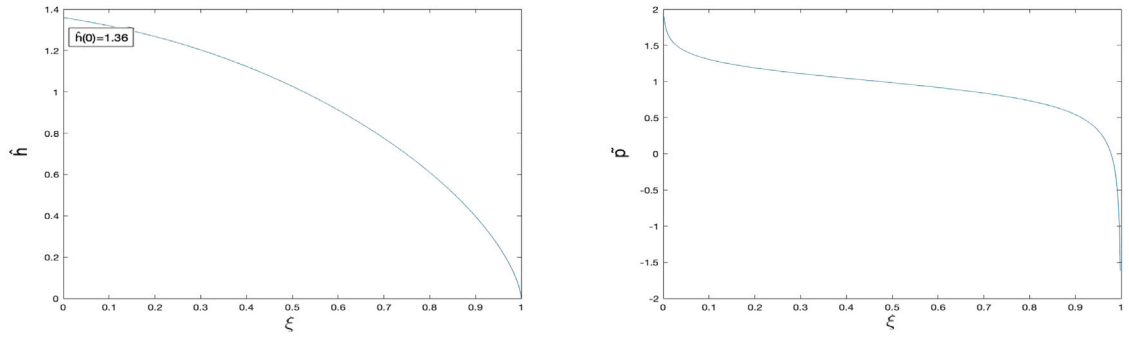
Fig. 4. (ξ, η) plots of $\tilde{h}$ and $\tilde{p}$, the scaled width and pressure solutions to the absorbed effective viscosity system.

Table 2
Test values of Π, μ_w and η_e.

Π	μ_w	η_e
0.05	487.3	2.74
0.20	23.35	3.92
0.40	3.93	10.37
0.55	1.06	96.60

Table 3
Values of A_i, B_i and Γ obtained using (40) with effective viscosity absorbed into the scaling and (29)–(32) with $\Pi \in \{0.05, 0.20, 0.40, 0.55\}$. We use $M = 500$ and $N = 4$ throughout.

Π	Absorbed	0.05	0.20	0.40	0.55
A_{-1}	0.14786	0.20710	0.23326	0.32238	0.67830
A_0	0.53529	0.74974	0.84444	1.16709	2.45559
A_1	0.01929	0.02702	0.03043	0.04206	0.08849
A_2	0.00402	0.00563	0.00634	0.00877	0.01844
A_3	0.00035	0.00049	0.00055	0.00076	0.00159
B_{-1}	0.14786	0.20710	0.23326	0.32238	0.67830
B_0	0.53805	0.75361	0.84879	1.17311	2.46825
B_1	0.05435	0.07612	0.08573	0.11849	0.24931
B_2	0.00012	0.00016	0.00019	0.00026	0.00054
B_3	0.00081	0.00114	0.00128	0.00177	0.00373
B_4	0.00029	0.00041	0.00046	0.00064	0.00134
Γ	0.59812	0.534579	0.513799	0.461261	0.359968

The latter columns of Table 3 show the values of A, B and Γ calculated using the exact method suggested in Section 6. Again we use $M + 1 = 501$ control points and $N = 4$. Happily, the same values are observed by using the values of A, B and Γ listed in the first column, calculated after absorbing the effective viscosity, and using the relations (39) to return to the concentration-specific values. We calculate the same value of $\Delta \approx 5 \times 10^{-5}$ each time; this is to be expected as the equations are equivalent once the solutions have been scaled.

Fig. 5 shows the distribution of proppants within the fracture for each value of Π. They are overlaid with an arrow plot of the proppant velocity profile, **v**, scaled by ξ to show the equivalent two-dimensional flux. The calculation of **v** is omitted since it is lengthy and similar to the derivation of (25) in Appendix A. As Π increases we see a growing disc of plug flow where $\phi > \phi_m$, marked with a magenta contour. The plug flow phenomenon has been observed in non-radial fracture geometries by Garagash (2014) and Dontsov and Peirce (2014b), so it is heartening to recover these results in the radial geometry. We also see a tendency towards proppant velocity across the crack, caused by the shear-induced migration of the proppants within the crack, as well as these fractures having greater height and smaller radius.

Drawing on calculations we have made so far, we are now in a position to assess the significance of tip screen-out in our model, something we have neglected so far by adopting a continuum model of proppant transport. This is where, near the crack tip, the narrowing crack aperture causes proppants to jam and block the fracture, significantly affecting the development of the evolving formation and the convective transport of proppants. In Dontsov and Peirce (2014b) this problem is addressed using a 'blocking function' which reduces proppant flux to zero in apertures smaller than three times the average particle's diameter. We will use this threshold to weigh the significance of ignoring screen-out in our model. Fig. 6a shows the volume-proportion of proppants predicted in fracture regions of width less than this threshold, dependent on the time, t, and the average proppant concentration, Π. We see that for early times and low concentrations, our model predicts a significant proportion of proppants in these regions, where the fracturing fluid is clear in reality, suggesting that tip screen-out is significant for these values. Indeed, in industrial fracturing a pad
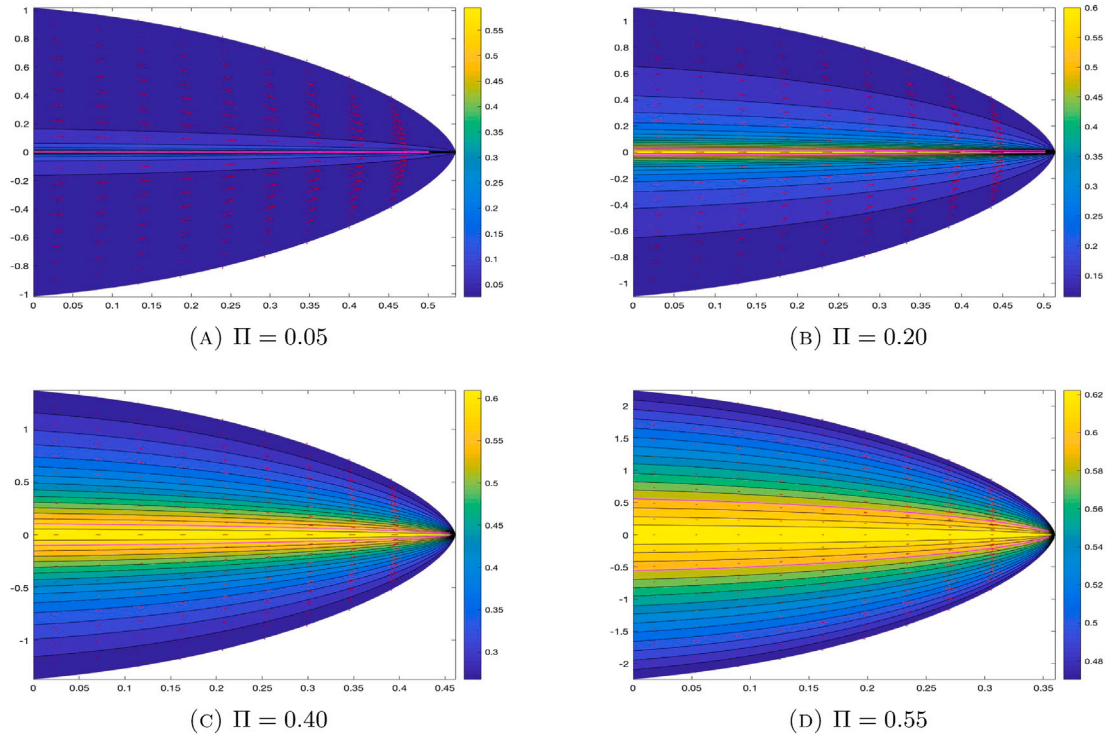
Fig. 5. Concentration-specific $(\Gamma\xi,\eta)$ plots of developing fractures with total solid volume fraction, Π, taking the values 0.05, 0.20, 0.40 and 0.55. These are presented with filled contours displaying proppant concentration; arrows showing ξ-scaled velocity; and magenta contours indicating the transition into plug flow at the centre of each cavity.

of clear fluid is injected ahead of the proppant to prevent early time jamming (Shiozawa and Mcclure, 2016), so this behaviour is not surprising. However, in concentrations greater than 0.4, where our densely fitted choice of rheology is most suitable, this proportion is relatively small; this means our model, which ignores tip screen-out, is suitable for modelling the distribution of proppants away from the crack tip. This difference arises from the effective viscosity, which increases with Π and causes the ratio of fracture width to length to decrease. Furthermore, for these greater concentrations, our calculations provide a simple and practical diagnostic for the total proportion of jammed proppants, which has clear applications in the industrial context.

Garagash (2014) conclude that their rheology, which is employed throughout this paper, agrees very well with experimental results when the predicted width of plug flow is greater than a particle's width, where it is less we can expect slight mismatches between predicted and practical concentration profiles; this arises from a breakdown of the continuum model in the jammed part of the flow (Garagash, 2014). In Fig. 6b, we see that, given we are interested in the $10^3 - 10^6$ s timescale (Shiozawa and Mcclure, 2016), these issues may be significant for low density flows where $\phi < 0.4$, but not for denser flows in the $\phi > 0.4$ range.

8. Conclusions

We have established a mathematical framework that captures the behaviour of a slurry within a pressure driven cavity. Using typical parameters from industrial fracking, we predict that the development length, required to establish stable proppant flow away from the wellbore, is negligible compared to the typical radius of the penny-shaped fracture generated. As a result, we may assume the flow is fully developed, reducing the in-fracture distribution of proppants to a function of the radial distance from the wellbore. A further assumption of constant proppant injection rate allows us to describe the proppant distribution with one parameter, the total solid volume fraction. In the zero-concentration limit, our model takes a very similar form to one derived by modelling the fracturing fluid as Newtonian, with some disagreement arising from our choice of a dense frictional rheology.

Within this framework, we are able to define an effective viscosity, which we may absorb into our equations using a suitable choice of scaling. This is a particularly striking result because it establishes an equivalence between slurry flow of a given solid fraction and simple Newtonian flow with some particular viscosity, at least in the sense of fracture development. Solving the resulting set of equations numerically, we may then return to our original scaling to investigate concentration-specific solutions. We recover width and pressure profiles with the tip-asymptotic behaviour described in the zero proppant model of Savitski and Detournay (2002). As the proppant concentration increases we expect thicker fractures with smaller radius and steeper fluid pressure gradients. In the centre of the fracture, where shear rate vanishes, we predict the formation of a disc of plug flow with width, in relation to the crack, increasing with the average proppant concentration. Our model has been successful in extending the main results of the
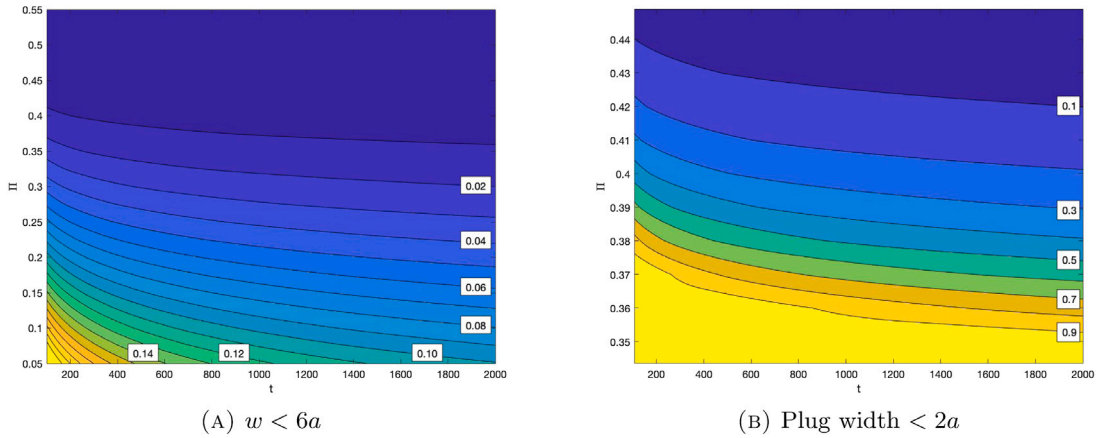
Fig. 6. Proportion of proppants by volume, predicted in fracture regions where $w < 6a$, or plug width $< 2a$, given average concentration, Π, and time, t.

modern hydraulic fracturing papers, Dontsov and Peirce (2014a, 2015) and Shiozawa and Mcclure (2016), to the lesser explored penny-shaped crack fracture geometry, using elegant power law scaling solutions. Evaluating our model, we see that the effect of tip screen-out is likely to be significant in the low concentration, low effective viscosity case, particularly at early times. For volume concentrations, $\Pi > 0.4$, we expect tip screen-out will have little effect on the development of the fracture except at the fracture tip, where we have developed diagnostics for the quantity of jammed proppant. Furthermore, with these greater concentrations, our model predicts plug flow which is thicker than one particle's width, so the results of Garagash (2014) suggest we should have good experimental agreement.

Lastly, in Appendices D and E, we have adopted a simple model of crack closure which regards the remaining proppants to be immobile and incompressible. This allows us to predict the shape of the residual crack, based on two parameters: the average proppant concentration within the injected fluid and the length of time between the initiation of fracking and the release of pressure. Simple formulae show that the residual fracture width increases significantly with proppant concentration, and grows very slowly with time; fracture radius however, decreases with proppant concentration and increases with time.

The results established here have important applications in both contexts of industrial fracking and geological dike formation. Diagnostics of tip screen-out and forecasts of residual fracture geometry are relevant to the formation of conductive fractures, whilst predictions about the shape and particle distribution of a slurry driven crack relate more to a cooling magma. The discovery of an effective viscosity may also provide a foothold in understanding slurry driven fractures, particularly given the bounty of literature surrounding cracks generated by Newtonian fluid. In spite of all this, experimental investigation is necessary to bolster the predictions we have made. We hope this will form the basis of a second article, with tentative title: 'Proppant flow in a penny-shaped crack. Part II : Experimental Investigation'.

Acknowledgements

Appendix A. Integrating the ϕ conservation equation over the crack width

In this Appendix we integrate equation (23) over $(-w, w)$ to yield (25); we will take a term-by-term approach. First, we note that by (22),

$$\int_{-z}^{z} \phi(\xi, \eta) d\eta = 2 \int_{0}^{z} \mu^{-1} \left(\mu_w(\xi) \frac{\eta}{w} \right) d\eta, \tag{41}$$

$$= 2z\Pi \left(\mu_w(\xi) \frac{z}{w} \right). \tag{42}$$

Hence, we see that

$$\int_{-w}^{w} \frac{\partial \phi}{\partial \xi} d\eta = \frac{\partial}{\partial \xi} \int_{-w}^{w} \phi d\eta - 2\phi(\xi, w) \frac{\partial w}{\partial \xi}, \tag{43}$$

$$= 2 \frac{\partial}{\partial \xi} \left[w \Pi \circ \mu_w(\xi) \right] - 2\phi(\xi, w) \frac{\partial w}{\partial \xi}. \tag{44}$$

Then, integrating by parts, we find

$$\int_{-w}^{w} \eta \frac{\partial \phi}{\partial \eta} d\eta = 2 \left[w\phi(\xi, w) - w\Pi \circ \mu_w(\xi) \right]. \tag{45}$$

Furthermore, utilising the expression of v_r given in (18) and the condition $v_r(\xi, \pm w) = 0$, we determine

$$\int_{-w}^{w} \frac{\partial(\xi \phi v_r)}{\partial \xi} d\eta = \frac{\partial}{\partial \xi} \left[\xi \int_{-w}^{w} \phi v_r d\eta \right], \tag{46}$$

$$= -\frac{6}{\Gamma} \frac{\partial}{\partial \xi} \left[\xi \frac{\partial p}{\partial \xi} \int_0^w \phi(\xi, \eta) \int_\eta^w \frac{I(\phi(\xi, z))z}{\mu(\phi(\xi, z))} dz d\eta \right], \tag{47}$$

$$= -\frac{6}{\Gamma} \frac{\partial}{\partial \xi} \left[\xi \frac{\partial p}{\partial \xi} \int_0^w \int_0^z \phi(\xi, \eta) \frac{I(\phi(\xi, z))z}{\mu(\phi(\xi, z))} d\eta dz \right], \tag{48}$$

$$= -\frac{6}{\Gamma} \frac{\partial}{\partial \xi} \left[\xi \frac{\partial p}{\partial \xi} \int_0^w z^2 \Pi \left(\frac{\mu_w z}{w} \right) \frac{I(\phi(\xi, z))}{\mu(\phi(\xi, z))} dz \right]. \tag{49}$$

However, by (22), $\mu(\phi(\xi, z)) = \mu_w z/w$, so

$$\int_{-w}^{w} \frac{\partial(\xi \phi v_r)}{\partial \xi} d\eta = -\frac{6}{\Gamma} \frac{\partial}{\partial \xi} \left[\frac{w\xi}{\mu_w} \frac{\partial p}{\partial \xi} \int_0^w z\Pi \left(\frac{\mu_w z}{w} \right) I \circ \mu^{-1} \left(\frac{\mu_w z}{w} \right) dz \right], \tag{50}$$

$$= -\frac{6}{\Gamma} \frac{\partial}{\partial \xi} \left[\frac{\xi w^3}{\mu_w(\xi)^2} \frac{\partial p}{\partial \xi} \Omega \circ \mu_w(\xi) \right]. \tag{51}$$

Finally, we know that

$$\int_{-w}^{w} \frac{\partial(\phi v_z)}{\partial \eta} d\eta = 2\phi(\xi, w)v_z(\xi, w). \tag{52}$$

In the original scaling we have the boundary condition $v_z(x, w) = \frac{\partial w}{\partial t}(x, t)$; in the lubrication scaling this becomes

$$-\dot{\epsilon}L v_z(\xi, w) = \left[\dot{\epsilon}L + \epsilon\dot{L} \right] w(\xi, T) - \epsilon L\xi \left[\frac{\dot{L}}{L} + \frac{\Gamma'\dot{T}}{\Gamma} \right] \frac{\partial w}{\partial \xi} + \dot{T}\frac{\partial w}{\partial T}. \tag{53}$$

Hence,

$$v_z(\xi, w) = \frac{w}{3} - \frac{4\xi}{3}\frac{\partial w}{\partial \xi}, \tag{54}$$

and so

$$\int_{-w}^{w} \frac{\partial(\phi v_z)}{\partial \eta} d\eta = 2\phi(\xi, w) \left[\frac{w}{3} - \frac{4\xi}{3}\frac{\partial w}{\partial \xi} \right]. \tag{55}$$

Adding these terms together and making various cancellations, we derive equation (25).

Appendix B. Zero-concentration limit

In this Appendix, we will compare the properties of Eq. (27) to the equivalent zero-proppant equation. Modelling the flow as Newtonian instead, we would have used the relation $\tau = \eta_f \dot{\gamma}$. In our choice of scaling this becomes $\tau = \dot{\gamma}$. Hence ((17).2) is replaced by

$$\frac{\partial v_r}{\partial \eta} = \frac{3\eta}{\Gamma}\frac{\partial p}{\partial \xi}, \tag{56}$$

where **v** is the fluid velocity. With the assumption that $\nabla \cdot v = 0$, our scaled continuity equation is simply

$$\frac{1}{\Gamma\xi}\frac{\partial(\xi v_r)}{\partial \xi} + \frac{\partial v_z}{\partial \eta} = 0. \tag{57}$$

Integrating first over $(-w, w)$ as in Appendix A, making use of (54), (56) and $\tau = \dot{\gamma}$, we obtain

$$\frac{w}{3} - \frac{4\xi}{3}\frac{\partial w}{\partial \xi} = \frac{1}{\xi\Gamma^2}\frac{\partial}{\partial \xi} \left[\frac{\partial p}{\partial \xi}\xi w^3 \right]. \tag{58}$$

Then, multiplying by ξ and integrating from ρ to 1, we use the $w^3 \partial p/\partial \xi \to 0$ limit employed to derive (27),

$$\int_\rho^1 \xi w d\xi + \frac{4}{9}\rho^2 w = -\frac{\rho w^3}{3\Gamma^2}\frac{\partial p}{\partial \rho}. \tag{59}$$

In order to compare (27) and (59), we are required to find the limit of $\Omega/(x^2\Pi)$ as $x \to \infty$. Explicitly we see that

$$\lim_{x \to \infty} \frac{\Omega(x)}{x^2\Pi(x)} = \lim_{x \to \infty} \frac{1}{x^3\Pi(x)} \int_0^x \Pi(u)I \circ \mu^{-1}(u)u du, \tag{60}$$

$$= \lim_{x \to \infty} \int_0^1 \frac{\Pi(vx)}{\Pi(x)} \cdot \frac{I \circ \mu^{-1}(vx)}{vx} \cdot v^2 dv, \tag{61}$$

Table 4
Matrix $(P)_{ij}$, for $N = 4$.

		\ j				
		−1	0	1	2	3
	−1	1.0000	0.0000	0.0000	0.0000	0.0000
	0	0.0000	0.9560	1.2730	0.4101	0.3145
i	1	0.0000	0.0991	−0.0185	0.4068	0.0610
	2	0.0000	0.0018	−0.0429	−0.0244	0.2293
	3	0.0000	0.0017	0.0039	−0.0416	−0.0141
	4	0.0000	0.0005	0.0026	−0.0032	−0.0372

$$= \int_0^1 v^2 \lim_{x \to \infty} \left[\frac{\Pi(vx)}{\Pi(x)} \right] dv, \tag{62}$$

$$= \int_0^1 v \lim_{x \to \infty} \left[\frac{\int_0^{vx} \mu^{-1}(u)du}{\int_0^x \mu^{-1}(u)du} \right] dv, \tag{63}$$

$$= \int_0^1 v^2 \lim_{x \to \infty} \left[\frac{\mu^{-1}(vx)}{\mu^{-1}(x)} \right] dv, \tag{64}$$

$$= \int_0^1 v^2 \lim_{x \to \infty} \left[\frac{I^{-1}(vx)}{I^{-1}(x)} \right] dv, \tag{65}$$

$$= \int_0^1 v^2 \lim_{x \to \infty} \left[\frac{1 + \sqrt{x}}{1 + \sqrt{vx}} \right] dv, \tag{66}$$

$$= \int_0^1 v^{3/2} dv, \tag{67}$$

$$= 2/5. \tag{68}$$

Here (62) and (65) arise from the fact $I(\phi) \sim \mu(\phi)$ as $\phi \to 0$, because the fluid shear stress approaches the slurry shear stress. (64) comes from L'Hôpital's rule. We conclude that the equations governing Newtonian flow are not the same as those in the zero-proppant slurry flow limit.

Appendix C. Matrix $(P)_{ij}$, when $N = 4$

The matrix $(P)_{ij}$ for $N = 4$, as provided in Savitski and Detournay (2002), is given in Table 4.

Appendix D. Crack closure: Problem formulation

In the zero-proppant case, Lai et al. (2016) have confirmed experimentally that for late times after the fluid pressure is released, meaning the net borehole pressure is effectively constant, the crack radius is constant and volume scales as $t^{-1/3}$. It is tempting to repeat our previous work in order to find an asymptotic solution with a generalised total fracture volume Qt^α. We would then let $\alpha = -1/3$ to model the case of closure. This approach leads us to

$$\alpha \int_\rho^1 \xi h(\xi) d\xi + \beta \rho^2 h = -\frac{\rho h^3}{\eta_e} \frac{\partial p}{\partial \rho}, \tag{69}$$

in the place of (38). Here $\beta = (3\alpha + 1)/9$ is the exponent for L, giving the radial growth of the fracture. However, we see that attempts to solve (69) using the previous numerical method fail as $(\alpha, \beta) \to (-1/3, 0)$, corresponding to the case in Lai et al. (2016). This is because the tip asymptotes $w \propto (1 - \xi)^{2/3}$ and $p \propto (1 - \xi)^{-1/3}$ are a result of an *advancing* fracture in a zero-toughness medium. Spence and Sharp (1985) note that $h \sim C(1 - \xi)^\tau$ implies $p \sim C\tau(\cot \pi\tau)(1 - \xi)^{\tau - 1}$. Balancing terms in (69), we are forced with $C \leq 0$ if $\beta \leq 0$ which clearly cannot lead to physical solutions, given the constraint $h \geq 0$. In the same paper, solutions for $\beta = 0$ are shown to exist without the assumption of zero-toughness; these have $h \sim (1 - \xi^2)^{1/2}$. However, this causes difficulties in the case of an evolving fracture, since a non-zero toughness parameter, $\aleph$, brings time dependence to the scaled equations we have derived. An alternative solution would be the addition of a non-zero fluid lag, providing a region of negative pressure between the fluid front and the crack tip. Such a region exists in reality, containing either vapour from the fracturing fluid or, if the surrounding medium is permeable, pore fluid (Rubin, 1993; Detournay and Garagash, 2003). Zero-toughness solutions using this formulation are explored in Garagash (2006). Schematics of each possible solution type are shown in Fig. 7.

Any model utilising a time independent concentration profile is likely to fail in describing fracture closure at late times. This is because the width of the crack is decreasing as $t^{-1/3}$, so it is bound to become comparable to the proppant diameter. At the point where $\epsilon L/a \approx 6$, the proppants begin to bridge across the fracture, effectively fixing them in position (Dontsov and Peirce, 2014b); therein, concentrations will increase as the carrier fluid is forced from the cavity. For this reason, we will instead address the problem of finding the residual crack shape, given some axisymmetric initial distribution of proppants; we will assume these are radially immobile from the moment pressure is released. This method has been used with success to model the closure of a bi-wing fracture by Wang et al. (2018) and Wang and Elsworth (2018).
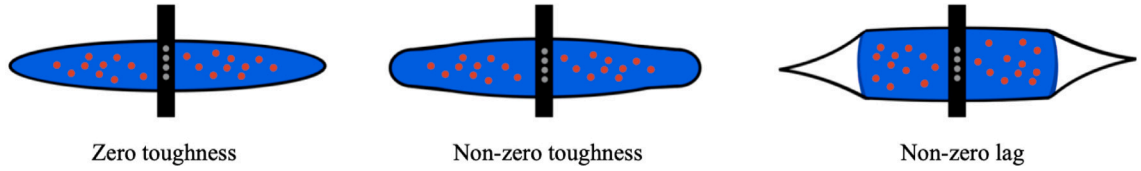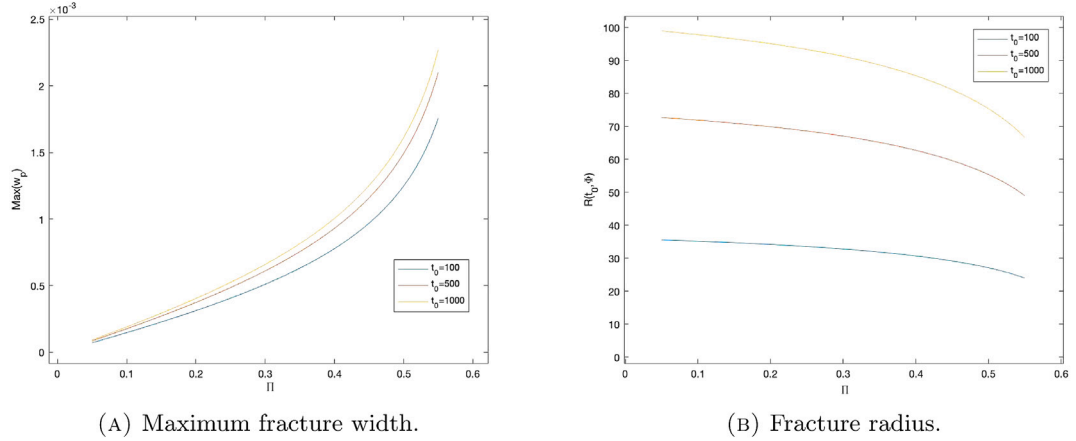
Fig. 7. Possibilities for modelling the crack tip.

(A) Maximum fracture width.

(B) Fracture radius.

Fig. 8. Plots showing the effect of average concentration on the maximum residual fracture width and radius for $t_0 \in \{100, 500, 1000\}$.

Appendix E. Crack closure: Residual width profiles

We model the residual shape of the fracture using $w_p(r)$, defined as the close packed width of proppants. That is to say, after packing the proppants as tightly as possible in the z direction, so $\phi = \phi_{rcp}$, this is the residual width. Given some radial distribution of proppants described by the average concentration, Π, and un-scaled width profile, w, we deduce that $w_p = w\Pi/\phi_{rcp}$. This description is compatible with the frictional rheology of Garagash (2014), used previously, which asserts that a non-zero normal force on the proppants, along with vanishing shear stress, causes compression up to the random close packing limit. We then assume that the surrounding fracture simply collapses around the proppant pack. Our primary interest will be in using proppant distributions, arising from the injection phase described previously, to predict the geometry of the residual formation.

In Wang and Elsworth (2018) a more complicated model is offered; this considers stress from the contact of opposing crack asperities, proppant embedment into the fracture walls, and compression of proppants. Since we will be concerned with cases where w_p is non-zero along the entire crack radius; the contact term arising from the crack asperities, which is significant in the un-propped case, will not be necessary. Furthermore, in the same paper (Wang and Elsworth, 2018) the depth of proppant embedment is shown to be of the order $K_e = a(3/4E')^2(16mE'^2/9c_p)^{2/3}$. Here, $m \approx 2\sqrt{3}$ is a constant which depends on the packing of proppants. Using the value of $c_p = 3.9 \times 10^{-8}$ Pa^{-1} (Wang and Elsworth, 2018), as well as the typical values of $a = 50$ μm and $E' = 40$ GPa mentioned earlier, we note that $K_e \approx 1$ μm, around 100 times smaller than the given proppant diameter. Since we will generally model proppant packs which are several times the size of the proppant diameter in width, we will ignore this phenomenon. Finally, we note that, according to our previous estimates, more than 10s into the injection phase we should expect pressures of less than 1 MPa. In Wang and Elsworth (2018) the compressive stress required to reduce the width of the closely packed proppant bed from w_p to w is given by $c_p^{-1} \ln(w_p/w)$; using this, the same stress would only cause a 4% reduction in width. Since typical stresses involved in the closure phase are much smaller than this, we will model the proppants as incompressible.

This model of crack closure leads to a simple description of the residual crack profile. We have two parameters: one for average concentration, Π, and another for the time that injection ceases, t_0. Herein we will denote $\{\tilde{h}, \tilde{p}, \tilde{\Gamma}\}$ as the solution to the system of equations given in (40); $\tilde{h}$ and $\tilde{p}$ are plotted in Fig. 4 and we use the value $\tilde{\Gamma} = 0.598$. Then, using (39) and the original scaling arguments, we deduce that

$$w_p(\xi; t_0, \Pi) = \frac{\Pi}{\phi_{rcp}} \epsilon(t_0) L(t_0) \eta_e(\Pi)^{2/9} \tilde{\Gamma} \tilde{h}(\xi), \tag{70}$$

$$R(t_0, \Pi) = L(t_0) \eta_e(\Pi)^{-1/9} \tilde{\Gamma}. \tag{71}$$

From Fig. 4 we notice that $\max(\tilde{h}_1) \approx 1.35$. Using this, we may plot Fig. 8a, which shows the effect of average concentration on the maximum residual width of the formation. It is interesting to note that the propped width does not grow proportional to the proppant concentration, as one may expect from the close packing of the suspended proppants. Instead, the dependence is superlinear, because

greater proppant concentrations lead to a higher effective viscosity; this causes the fracture to take a wider shape before the release of injection pressure. We can also see that t_0 has relatively little effect on the maximum crack width. This is because the t_0 dependent term, ϵL, grows with $t_0^{1/9}$. By contrast, in Fig. 8b we see a greater time dependence in the final radius, which grows with $L \propto t^{4/9}$. As the proppant concentration increases, with t_0 fixed, we see a decrease in the final radius of fracture achieved, arising from an increase in the effective viscosity.

References

Abramowitz, M., Stegun, I.A. (Eds.), 1964. HandBook of Mathematical Functions with Formulas, Graphs, and Mathematical Tables. In: Applied Mathematics Series, vol. 55, US Govt. Print. Off, Washington, DC.

Bacri, J.-C., Frenois, C., Hoyos, M., Perzynski, R., Rakotomalala, N., Salin, D., 1986. Acoustic study of suspension sedimentation. Europhys. Lett. 2 (2), 123–128.

Belyadi, Hoss, Fathi, Ebrahim, Belyadi, Fatemeh, 2019. Chapter fifteen - numerical simulation of hydraulic fracturing propagation. In: Belyadi, Hoss, Fathi, Ebrahim, Belyadi, Fatemeh (Eds.), Hydraulic Fracturing in Unconventional Reservoirs, second ed. Gulf Professional Publishing, ISBN: 9780128176658, pp. 257–272. http://dx.doi.org/10.1016/B978-0-12-817665-8.00015-1.

Boyer, F., Guazzelli, É., Pouliquen, O., 2011. Unifying suspension and granular rheology. Phys. Rev. Lett. 107 (18), 188301.

Charlez, Philippe A., 1997. Rock Mechanics: Petroleum Applications. Editions Technip, Paris, ISBN: 9782710805861, p. 239.

Dagois-Bohy, S., Hormozi, S., Guazzelli, É., Pouliquen, O., 2015. Rheology of dense suspensions of non-colloidal spheres in yield-stress fluids. J. Fluid Mech. 776, R2. http://dx.doi.org/10.1017/jfm.2015.329.

Detournay, E., Garagash, D., 2003. The tip region of a fluid-driven fracture in a permeable elastic solid. J. Fluid Mech. 494, 1–32.

Dontsov, EV., Boronin, SA., Osiptsov, AA., Derbyshev, DY., 2019a. Lubrication model of suspension flow in a hydraulic fracture with frictional rheology for shear-induced migration and jamming. Proc. R. Soc. Lond. Ser. A Math. Phys. Eng. Sci. 475, 20190039.

Dontsov, EV., Boronin, SA., Osiptsov, AA., Derbyshev, DY., 2019b. Lubrication model of suspension flow in a hydraulic fracture with frictional rheology for shear-induced migration and jamming. Proc. R. Soc. Lond. Ser. A Math. Phys. Eng. Sci. 475, 20190039.

Dontsov, E.V., Peirce, A.P., 2014a. The effect of proppant size on hydraulic fracturing by a slurry. In: 48th US Rock Mechanics / Geomechanics Symposium, Minneapolis. American Rock Mechanics Association.

Dontsov, E.V., Peirce, A.P., 2014b. Slurry flow, gravitational settling and a proppant transport model for hydraulic fractures. J. Fluid Mech. 760, 567–590.

Dontsov, E.V., Peirce, A.P., 2015. Proppant transport in hydraulic fracturing: Crack tip screen-out in KGD and P3D models. Int. J. Solids Struct. 63, 206–218. http://dx.doi.org/10.1016/j.ijsolstr.2015.02.051.

Einstein, A., 1906. A new determination of molecular dimensions. Ann. Phys 4 (19), 289–306.

Garagash, D., 2006. Propagation of a plane-strain hydraulic fracture with a fluid lag: Early-time solution. Int. J. Solids Struct. 43, 5811–5835.

Garagash, Lecampion, 2014. Confined flow of suspensions modelled by a frictional rheology. J. Fluid Mech. 759, 197–235. http://dx.doi.org/10.1017/jfm.2014.557, 2014, 2014, Cambridge University Press.

Garagash, D.I., Detournay, E., 2000. The tip region of a fluid-driven fracture in an elastic medium. ASME J. Appl. Mech. 67, 183–192.

Garside, J., Al-Dibouni, M.R., 1977. Velocity-voidage relationships for fluidization and sedimentation in solid–liquid systems. Ind. Eng. Chem. Process Des. Dev. 16 (2), 206–214.

Lagarias, J.C., Reeds, J.A., Wright, M.H., Wright, P.E., 1998. Convergence properties of the nelder–mead simplex method in low dimensions. SIAM J. Optim. 9 (1), 112–147, 1998.

Lai, Ching-Yao, Zheng, Zhong, Dressaire, Emilie, Ramon, Guy Z., Huppert, Herbert E., Stone, Howard A., 2016. Elastic relaxation of fluid-driven cracks and the resulting backflow. Phys. Rev. Lett. 117, 268001.

Liang, Feng, Sayed, Mohammed, Al-Muntasheri, Ghaithan A., Chang, Frank F., Li, Leiming, 2016. A comprehensive review on proppant technologies. Petroleum 2 (1), 26–39.

Miller, Bruce G., 2005. Coal Energy Systems. In: Sustainable World Series, Academic Press, ISBN: 9780124974517, p. 380.

National Earthquake Hazards Reduction Program (U.S.), Geological Survey (U.S.), 1983. Office of earthquakes, volcanoes, and engineering. In: Hydraulic Fracturing Stress Measurements. Vol. 26, U.S. National Committee for Rock Mechanics, International Journal of Rock Mechanics and Mining Sciences and Geomechanics Abstracts.

O'Keeffe, Niall J., Huppert, Herbert E., Linden, P.F., 2018. Experimental exploration of fluid-driven cracks in brittle hydrogels. J. Fluid Mech. 844, 435–458.

Petford, N., Koenders, M.A., 1998. Granular flow and viscous fluctuations in low bagnold number granitic magmas. J.Geol. Soc. 155 (5), 873–881. http://dx.doi.org/10.1144/gsjgs.155.5.0873.

Pierce, Brenda, 2010. Geothermal Energy Resources. National Association of Regulatory Utility Commissioners (NARUC).

Rice, J.R., 1968. Mathematical analysis in the mechanics of fracture. In: Liebowitz, H. (Ed.), Fracture, an Advanced Treatise. II. Academic Press, New York, NY, pp. 191–311, (Chapter 3).

Richardson, J., Zaki, W., 1954. Sedimentation and fluidization: Part i. Trans. Inst. Chem. Eng. 32, 35–47.

Rivalta, E., Taisne, B., Bunger, A.P., Katz, R.F., 2015. A review of mechanical models of dike propagation: Schools of thought, results and future directions. Tectonophysics (ISSN: 0040-1951) 638, 1–42, 2015.

Rubin, A.M., 1993. Tensile fracture of rock at high confining pressure: implications for dike propagation. J. Geophys. Res. 98 (B9), 15, 919–15, 935, 1993.

Savitski, A.A., Detournay, E., 2002. Propagation of a penny-shaped fluid-driven fracture in an impermeable rock: asymptotic solutions. Int. J. Solids Struct. 39 (26), 6311–6337.

Shiozawa, S., Mcclure, M., 2016. Simulation of proppant transport with gravitational settling and fracture closure in a three-dimensional hydraulic fracturing simulator. J. Petrol. Sci. Eng. 138, 298–314.

Sneddon, I.N., 1951. Fourier Transforms. McGraw-Hill, New York, NY.

Spence, D.A., Sharp, P.W., 1985. Self-similar solution for elastohydrodynamic cavity flow. Proc. R. Soc. Lond. Ser. A (400), 289–313.

Wang, J., Elsworth, D., 2018. Role of proppant distribution on the evolution of hydraulic fracture conductivity. J. Petrol. Sci. Eng. 166, 249–262.

Wang, Jiehao, Elsworth, Derek, Denison, Martin K., 2018. Propagation, proppant transport and the evolution of transport properties of hydraulic fractures. J. Fluid Mech. 855, 503–534.

Wells, Bruce A. (Ed.), 2007. Shooters. the Petroleum Age. 4, American Oil and Gas Historical Society, pp. 8–9, (3), ISSN 1930-5915.

Zhang, Xi, Wu, Bisheng, Jeffrey, Robert G., Connell, Luke D., Zhang, Guangqing, 2017. A pseudo-3D model for hydraulic fracture growth in a layered rock. Int. J. Solids Struct. (ISSN: 0020-7683) 115–116, 208–223. http://dx.doi.org/10.1016/j.ijsolstr.2017.03.022, http://www.sciencedirect.com/science/article/pii/S0020768317301312.

Zhixi, Chen, Mian, Chen, Yan, Jin, Rongzun, Huang, 1997. Determination of rock fracture toughness and its relationship with acoustic velocity. Int. J. Rock Mech. Min. Sci. (ISSN: 1365-1609) 34 (3–4), 49.e1–49.e11.